Journal of Mechanical Design. Received November 21, 2019;
Accepted manuscript posted March 14, 2020. doi:10.1115/1.4046810

Zero Torque Compliant Mechanisms Employing Pre-Buckled Beams

Pietro Bilancia*
Dept. of Mechanical, Energy, Management and Transportation Engineering
University of Genova
Genova, Italy 16145
Email: pietro.bilancia@edu.unige.it

Samuel P. Smith
Dept. of Mechanical Engineering
Brigham Young University
Provo, Utah 84602
Email: samportersmith@byu.edu

Giovanni Berselli
Dept. of Mechanical, Energy, Management and Transportation Engineering
University of Genova
Genova, Italy 16145
Email: giovanni.berselli@unige.it

Spencer P. Magleby
Dept. of Mechanical Engineering
Brigham Young University
Provo, UT 84602
Email: magleby@byu.edu

Larry L. Howell
Dept. of Mechanical Engineering
Brigham Young University
Provo, UT 84602
Email: lhowell@byu.edu

The concept of a statically balanced mechanism with a single rotational degree of freedom is presented. The proposed device achieves static balancing by combining positive stiffness elements and negative stiffness elements within an annular domain. Two designs are discussed. The first is composed of an Archimedean spiral and two pinned-pinned prebuckled beams. The overall mechanism is modeled via an analytical approach and the element dimensions are optimized. The optimal configuration is then tested through finite element analysis (FEA). A second approach replaces the spiral beam with elastic custom-shaped spline beams. A FEA optimization is performed to determine the shape and size of such spline beams. The behavior of the negators is used as reference for the optimization so as to achieve a complete balancing. A physical prototype of each configuration is machined and tested. The comparison between predicted and acquired data confirmed the efficacy of the design methods.

1 Introduction

Constant torque compliant mechanisms (CMs) [1] are devices that provide a near constant output torque for a certain range of angular inputs [2–7]. Different than the constant torque springs presented in [8], constant torque CMs are characterized by a single common axis of rotation between the input and output frames. In practice, they may be envisaged as the rotational counterpart of constant force CMs, which have been thoroughly studied and optimized in the previous literature [9–17]. Potentially, constant torque CMs can supply a variety of desirable qualities, including absence of backlash and friction, reduced part count, and easier assembly. They can also be used to realize compact and rather simple mechatronic systems requiring torque regulation, since no controllers or sensors are needed to maintain a specific torque value. Examples of applications include rehabilitative and assisting devices [2], medical tools [3], aerospace devices [18] and counterbalancing systems in robotic arms [19, 20].

In the literature, different methods are available for synthesizing constant torque CMs. For instance, a possible method is to employ bistable beams, whose behavior has been extensively studied [9, 17, 21, 22]. According to the results reported in [23, 24], a fixed-guided beam can be used either as a negative stiffness structure to be combined with a classical positive stiffness structure (many examples can be viewed in [17]) or, under specific circumstances, as a structure capable of producing a constant output itself, as shown in [7]. The latter method leads to a single-piece solution, though the resulting constant output is available only for a limited angular range. An extended range is achieved in [2–5], where the intrinsic zero stiffness behavior is obtained via a set of elastic curved beams that connect an in-

Journal of Mechanical Design. Received November 21, 2019;
Accepted manuscript posted March 14, 2020. doi:10.1115/1.4046810

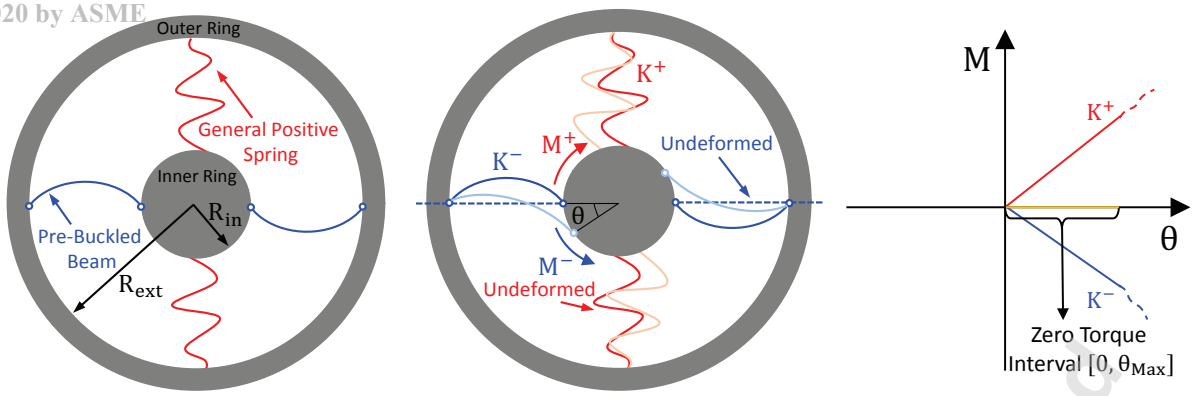

(a) General architecture. (b) Deformed configuration. (c) Stiffness compensation.

Fig. 1: Conceptual schematic of the zero torque CM.

ner (movable) ring to an outer (fixed) ring. The shape of the beams is optimized so as to provide a pre-defined torque level over a large range of angular deflections. However, the resulting monolithic solution is affected by a pre-loading range (i.e. it has to be pre-loaded in order to function as a constant torque device), usually amounting to one-third of the total angular range. This issue has been overcome in [6], in which the post-buckling behavior of initially straight beams is used to produce a constant torque through the entire range.

Despite their stiffness is null for a definite range of angular displacements, constant torque CMs require external actuation to deflect the flexible members and to maintain the deformed state. In particular, employing the same terminology of [25], the spring-back behavior can be avoided by designing statically balanced CMs [26–30]. These devices combine the benefits of CMs with some benefits of conventional rigid mechanisms, namely absence of a preferential equilibrium position and absence of undesired energy storage [25]. Indeed, note that CMs characterized by a positive stiffness always require an increasing actuation force/torque to generate large displacements, which is not the case for the statically balanced CMs. Hence, from a practical standpoint, their implementation may be beneficial for reducing the actuation effort [28], allowing for smaller and lighter actuators. In the recent literature, a number of architectures for statically balanced CMs employing the cross-axis flexural pivot concept have been presented [25, 31, 32]. Many of these systems achieve significant angular deflections (see [25], where the null output is available for 1.4 rad of rotation), however, these mechanisms are rather unpractical due to their large size. Moreover, the cross-axis pivot is subjected to an undesired axis shift (i.e. parasitic motion [33]) during the deflection [34, 35].

A possible way to overcome these issues may be the use of the hereby named zero torque CMs. These are a special class of statically balanced CMs, characterized by a single rotational degree of freedom. Referring to Fig. 1, the zero torque CM proposed hereafter is composed of two concentric rings, one fixed and one movable. If a pure rotation is applied to the movable ring and other external disturbances (parasitic loads [33]) are neglected, the system will react with a negligible torque and a null axis shift. However, differently from e.g. C-Flex bearings [36], also referred to as tubular CAFP in [37], the zero torque CMs cannot support radial loads, unless a properly defined constraint set is provided to the rings (as it will be shown in Sec. 2). Due to their compactness and scalability, zero torque CMs may be used as substitutes for traditional rotational joints in mechanical systems that need reduced part number or reduced friction. For instance, they may be considered during the initial CM design phase when applying the rigid-body replacement method [38]. Envisaged applications concern small manipulators, such as tendon driven robotic fingers [33, 39].

From a design standpoint, a zero torque CM can be realized by means of the stiffness compensation method [40, 41], i.e. by combining purposely conceived elements capable of reciprocally balance their action during the motion of the system, as shown in Fig. 1. The overall mechanism is then composed by positive stiffness members (denoted with K^+ in Fig. 1(b)) and by negative stiffness members (denoted with K^- in Fig. 1(b), hereinafter referred to as negators). Differently from the above-mentioned constant force/torque CMs, which make use of initially straight bistable beams, here the negators are pre-buckled and thus the stiffness compensation is achieved without an initial force/torque offset. In fact, as shown in [23, 24], bistable beams behave as positive stiffness springs in the first range of deflections. Generally speaking, fixed-fixed beams, also largely employed when realizing constant force linear CMs (see, e.g., [9, 12, 17]), seem preferable as they allow one-piece solutions. On the other hand, their application to the annular domain (as the one presented in this paper) is quite limited due to the critical stress condition arising in the beams when large rotations between the rings are enforced. Also, fixed-fixed beams show an asymmetric behavior for positive and negative rotations due to evident differences in the deformed shapes. Based on the results reported in [15, 22], pinned-pinned pre-buckled beams are adopted as negators in this work due to their symmetric behavior and lower stress.

As a drawback, the use of pinned-pinned pre-buckled

beams does not allow to obtain jointless CMs. As previously stated, another limit of the zero torque CMs is the rather limited resistance when subjected to radial loads. Moreover, as a CM, the available angular range is limited by the stress arising in the CM and by the negators operability. At last, fatigue life of the flexible members requires special attention and, depending on the application, may represent a critical issue.

On the basis of these considerations and the conceptual schematic reported in Fig. 1, this paper reports the design of a compact zero torque CM with annular configuration. Two different solutions are analyzed and discussed in this paper. The first design exploits the Archimedean spiral [8,42,43] as a torsional element that undergoes large angular deflections with a constant positive stiffness (K^+). Analytical behavioral models for both the negator and the spiral are provided. The size of the elements is obtained via an optimization routine carried out in Matlab, and verified by means of finite element analysis (FEA) conducted in ANSYS. Then, as an attempt to increase the compensation accuracy and to further limit the dimensions of the overall mechanism, a second design is pursued by implementing custom shaped spline beams in place of the previous spiral. The shape and size of such beams are optimized via FEA to match a pre-defined behavior [44,45], obtained by reversing the negator's characteristic in the positive plane. Finally, physical prototypes of both the configurations are fabricated in polypropylene via CNC machining and their performance is tested using a rotational setup. The negators are cut from a sheet of spring steel.

The design process and the experimental validation are hereinafter illustrated. The paper is organized as follows: Sec. 2 reports the analytical modeling of the zero torque CM, Sec. 3 describes the adopted design procedure and its practical implementation in a multi-software environment, Sec. 4 reports on the FEA shape optimization carried out to increase the mechanism accuracy, whereas Sec. 5 shows the experimental investigations. The concluding remarks are given in Sec. 6.

2 Analytical Modeling of the Zero Torque Mechanism

This section provides the analytical modeling of the first design utilizing an Archimedean spiral and pinned-pinned pre-buckled beams. The two opposing inputs are analyzed separately to underline the influence of the parameters on the resulting stiffnesses. Then, by combining the equations, the expression of the overall mechanism torque is obtained and subsequentially used in the size optimization problem.

2.1 Archimedean Spiral Torsion Spring

The Archimedean spiral has been used extensively as a compliant transmission element [42, 43, 46, 47] due to evident design advantages, including simple analytical formulations which accurately predict the spring behavior and quasi-constant stiffness availabilities for a wide angular range. The spiral can be easily adapted to the annular domain considered in this work. With reference to Fig. 2, by adopting a polar coordinate system (R, α), and then selecting number of turns, n_t, and inner/outer ring radii, R_{in} and R_{ext}, the location

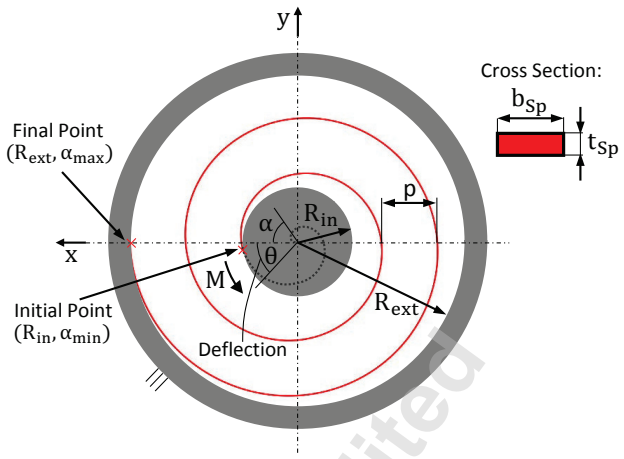

Fig. 2: Archimedean spiral geometry in the annular frame.

of the initial and final points of the spiral, namely (R_{in}, α_{min}) and (R_{ext}, α_{max}), can be found by means of the following relations [43]:

$$\alpha_{max} = 2\pi n_t \tag{1}$$

$$p = \frac{2\pi R_{ext}}{\alpha_{max}} \tag{2}$$

$$\alpha_{min} = \frac{2\pi R_{min}}{p} \tag{3}$$

where p is the pitch between the coils. The shape of the spiral, to be defined between (R_{in}, α_{min}) and (R_{ext}, α_{max}), can be obtained as follows:

$$R(\alpha) = \frac{p\alpha}{2\pi} \tag{4}$$

$$x = R\cos(\alpha) \tag{5}$$

$$y = R\sin(\alpha) \tag{6}$$

To calculate the rotational stiffness, the length of the flexible element must be determined. As highlighted in Fig. 2, the central portion of the spiral is considered part of the rigid inner ring. Therefore, with respect to the central coordinate system, the characteristic spring length is given by:

$$L_{Sp} = L_{tot} - L_{in} \tag{7}$$

where

$$L_{tot} = \frac{p}{4\pi}\left[\alpha_{max}\sqrt{1+\alpha_{max}^2} + \ln\left(\alpha_{max}\sqrt{1+\alpha_{max}^2}\right)\right] \tag{8}$$

$$L_{in} = \frac{p}{4\pi}\left[\alpha_{min}\sqrt{1+\alpha_{min}^2} + \ln\left(\alpha_{min}\sqrt{1+\alpha_{min}^2}\right)\right] \tag{9}$$

If a rectangular cross section, such as the one in Fig. 2 de-

Journal of Mechanical Design. Received November 21, 2019;
Accepted manuscript posted March 14, 2020. doi:10.1115/1.4046810

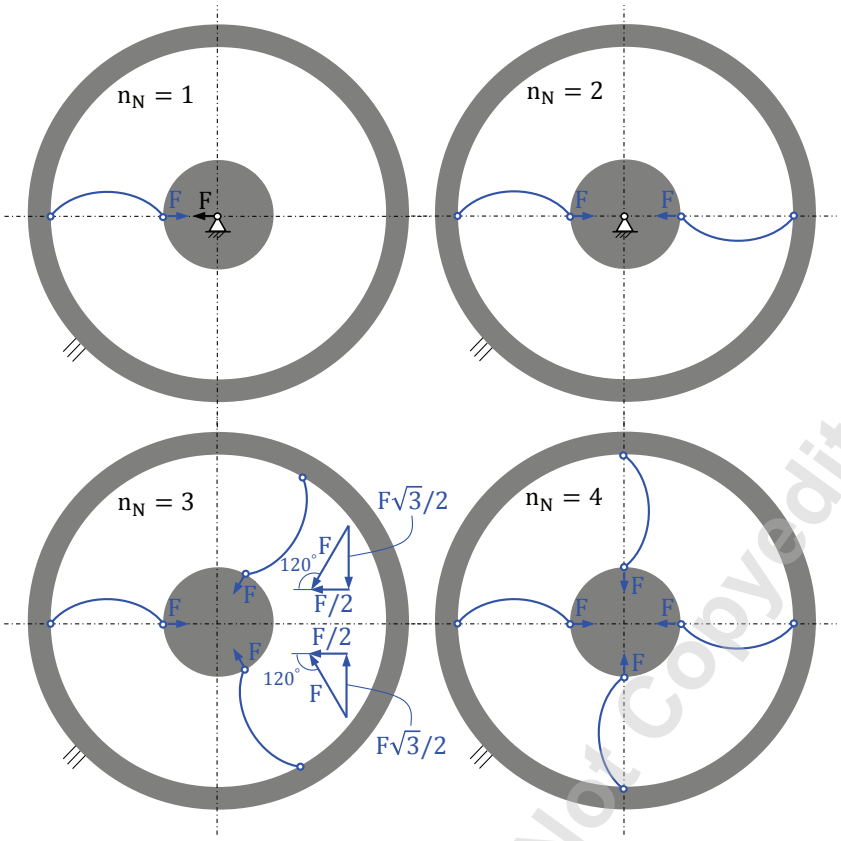

Fig. 3: Pinned-pinned pre-buckled negators in the annular frame.

fined by width b_{Sp} and thickness t_{Sp}, is considered, the spring rotational stiffness along the z-axis becomes [42]:

$$k_{Sp} = \frac{E_{Sp} b_{Sp} t_{Sp}^3}{12 L_{Sp}} \tag{10}$$

E_{Sp} being the material elastic modulus. The spring reaction torque for an imposed angular deflection θ is given by:

$$M_{Sp} = k_{Sp}\theta \tag{11}$$

and the maximum stress acting on the coils can be found as [42]:

$$\sigma_{Sp} = \frac{6 M_{Sp}}{b_{Sp} t_{Sp}^2} \tag{12}$$

When large rotations are enforced, undesired contacts may occur between the spiral and the inner ring. However, such contacts can be avoided by purposely shaping the inner ring.

2.2 Pre-Buckled Negator

The proposed zero torque CM comprises a set of n_N negators arranged in a parallel spring configuration within the annular domain to provide the required compensation. Provided the beams are equally spaced in the angular domain, n_N can be arbitrarily selected while still preserving equilibrium in the initial configuration and thus during assembly. Except for $n_N = 1$, which requires a central pin to constrain the translation along the horizontal axis, the equally spaced parallel configurations ensure force and torque balancing in the initial state ($\theta = 0$ rad). In practice, the central pin is adopted also for $n_N = 2$, as visible in Fig. 3, in order to avoid instability along the vertical axis.

In this section, the behavior of a single pre-buckled beam in the annular domain is analyzed, as visible in the principle schematic of Fig. 4. The effect of varying n_N will be considered in Sec. 2.3. The negator is simply a pinned-pinned straight beam with a constant rectangular cross section along the main axis. Its geometry is defined by length L_N, width b_N and thickness t_N, as shown in Figs. 4(a)-4(b). Referencing Fig. 4(b) as well as the theory reported in [22], the behavioral modeling of the beam under axial loads beyond the buckling load, $F_{cr} = \pi^2 E_N I_N / L_N^2$, E_N being the material elastic modulus and $I_N = b_N t_N^3/12$ the cross section's moment of inertia, can be solved in closed-form resulting in the following relations:

Journal of Mechanical Design. Received November 21, 2019;
Accepted manuscript posted March 14, 2020. doi:10.1115/1.4046810

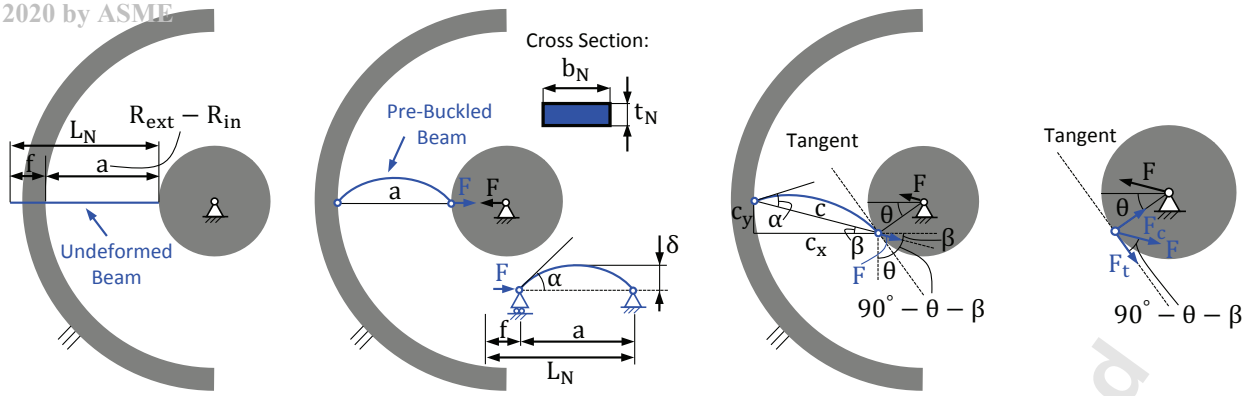

(a) Initial configuration. The straight flexible beam is unloaded. (b) Pre-loaded condition. An axial displacement f is imposed to deflect the beam and realize the pinned-pinned condition. (c) Working condition. An angular displacement θ is imposed to the inner ring. (d) Detailed view: resulting forces transmitted to the inner ring.

Fig. 4: Principle schematic of the pre-buckled negator.

$$\frac{f}{L_N} = \frac{L_N - a}{L_N} = 2\left(1 - \frac{E(\alpha)}{K(\alpha)}\right) \tag{13}$$

$$\frac{F}{F_{cr}} = \frac{4K(\alpha)^2}{\pi^2} \tag{14}$$

$$\frac{\delta}{L_N} = \frac{\sin(\alpha/2)}{K(\alpha)} \tag{15}$$

$$\frac{M_{fmax}}{F_{cr}L_N} = \frac{4\sin(\alpha/2)K(\alpha)}{\pi^2} \tag{16}$$

where f is the axial displacement of the movable pin, $a = R_{ext} - R_{in}$ is the distance between the pins in the deformed configuration, δ is the maximum transversal displacement of the beam, M_{fmax} is the maximum bending moment acting on the beam, and α is the end rotation of the beam under load. The quadratic functions $E(\alpha) = \pi/2 - 0.1\alpha^2$ and $K(\alpha) = \pi/2 + 0.1\alpha^2$ are used in place of the complete elliptic integrals of the first and second kind [48] to ensure the closed-form of the problem. By imposing a rotation θ to the inner ring (see Fig. 4(c)), the distance between the pins can be expressed as:

$$c = \sqrt{c_x^2 + c_y^2} = \sqrt{(a - R_{in}(\cos(\theta) - 1))^2 + R_{in}^2 \sin^2(\theta)} \tag{17}$$

By introducing Eq. 17 in Eq. 13 (where a becomes c), it is possible to derive the following expression for α:

$$\alpha = \pm\sqrt{5\pi}\sqrt{\frac{L_N - c}{3L_N + c}} = \pm\sqrt{5\pi}\sqrt{\frac{L_N - \sqrt{(a - R_{in}(\cos(\theta) - 1))^2 + R_{in}^2\sin^2(\theta)}}{3L_N + \sqrt{(a - R_{in}(\cos(\theta) - 1))^2 + R_{in}^2\sin^2(\theta)}}} \tag{18}$$

Equation 18 can be substituted in $K(\alpha)$ and thus entered in Eq. 14 to find the following solution for F:

$$F = \frac{16E_N I_N \pi^2}{(3L_N + c)^2} = \frac{16E_N I_N \pi^2}{\left(3L_N + \sqrt{(a - R_{in}(\cos(\theta) - 1))^2 + R_{in}^2\sin^2(\theta)}\right)^2} \tag{19}$$

Referring to Fig. 4(d), the torque generated by the negator can be written as:

$$M_N = F_t R_{in} = F\cos(\pi/2 - \theta - \beta)R_{in} \tag{20}$$

where

$$\theta = \arctan\left(\frac{R_{in}\sin(\theta)}{a + R_{in} - R_{in}\cos(\theta)}\right) \tag{21}$$

The maximum stress acting on the beam is reached in the pre-loaded condition (i.e. for $\theta = 0$). In this configuration, being $f = L_N - a$ (see Fig. 4(b)), the following expression for α can be directly obtained from Eq. 13:

$$\alpha = \pm\sqrt{5\pi}\sqrt{\frac{f}{4L_N - f}} \tag{22}$$

By introducing Eq. 22 in $K(\alpha)$ and then substituting $K(\alpha)$ in Eq. 16, the following expression for M_{fmax} holds:

$$M_{fmax} = \frac{8\pi E_N I_N \sin\left(\frac{\sqrt{5\pi}\sqrt{f/(4L_N - f)}}{2}\right)}{4L_N - f} \tag{23}$$

Therefore, the maximum stress due to bending can be determined as [22]:

$$\sigma_N = \frac{6M_{fmax}}{b_N t_N^2} \tag{24}$$

2.3 Optimization Problem

The overall mechanism combines the previous concepts. The spiral and the negators are arranged in two parallel planes to avoid mutual interactions. The resulting torque generated for an imposed rotation θ is given by:

$$M = M_{Sp}(E_{Sp}, b_{Sp}, t_{Sp}, L_{Sp}) - n_N M_N(E_N, b_N, t_N, L_N) \tag{25}$$

When designing the proposed mechanism, R_{in} and R_{ext} should be considered as input parameters for the problem because they vary depending on the application. This applies to the material selection (E_{Sp} and E_N) as well as to the number of negators, n_N. Since $L_{Sp} = L_{Sp}(R_{in}, R_{ext}, n_t)$ and $L_N = L_N(R_{in}, R_{ext}, f)$ (see Eqs. 9 and Fig. 4(b)), the design variables become:

- b_{Sp}, t_{Sp}, b_N and $t_N \rightarrow$ cross sections' dimensions;
- $n_t \rightarrow$ number of spiral's turns;
- $f \rightarrow$ initial axial displacement for the negator(s).

Knowing the angular range $[0, \theta_{max}]$ to be considered and the materials' yield strength, $\sigma_{max,Sp}$ and $\sigma_{max,N}$, the optimization problem may be formalized as follows:

$$\textbf{Min.}\ M_{rms} = \sqrt{\frac{1}{r}\sum_{i=1}^{r}\left[M_{Sp_i} - n_N M_{N_i}\right]^2} \tag{26}$$

$$\textbf{Constraints} \rightarrow \begin{cases} \sigma_{Sp} < \sigma_{max,Sp} \\ \sigma_N < \sigma_{max,N} \end{cases} \tag{27}$$

$$\textbf{DesignVar.} \rightarrow \begin{cases} b_{Sp} \in [b_{Sp,min}, b_{Sp,max}] \\ t_{Sp} \in [t_{Sp,min}, t_{Sp,max}] \\ b_N \in [b_{N,min}, b_{N,max}] \\ t_N \in [t_{N,min}, t_{N,max}] \\ n_t \in [n_{t,min}, n_{t,max}] \\ f \in [f_{min}, f_{max}] \end{cases} \tag{28}$$

where M_{rms} is the root mean square (rms) value of the mechanism torque (see Eq. 25), evaluated by varying θ in a series of r incremental step within the range $[0, \theta_{max}]$. The imposed constraints preserve the structural integrity of the members in the operative range. To ensure the correct negators' operability in $[0, \theta_{max}]$, the total length L_N must be higher than a minimum value. Being $L_N = a + f = (R_{ext} - R_{in}) + f$, this condition can be imposed to f_{min}. With reference to Fig. 4(c) and to Eq. 17, for a maximum deflection angle equal to θ_{max}, it is possible to write:

$$f_{min} = c(\theta_{max}) - a = \sqrt{\left(a - R_{in}\left(\cos(\theta_{max}) - 1\right)\right)^2 + R_{in}^2 \sin^2(\theta_{max})} - a \tag{29}$$

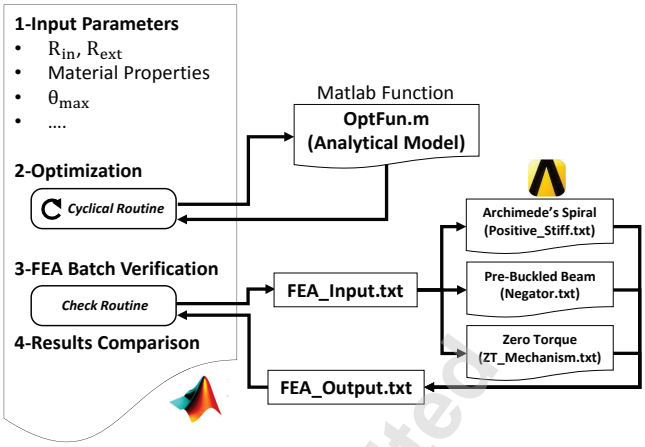

Fig. 5: Multi-software design tool.

3 Design of Zero Torque Mechanisms

This section provides a detailed overview of the proposed design approach and describes its software implementation. The overall system, which provides $M = 0$ in the range $[0, \theta_{max}]$, has been conceived as a combination of two annular frames: the first frame accommodates the spiral and the second frame comprises a set of $n_N = 2$ negators (see Figs. 2-3). The frames are then rigidly connected to each other at the inner and outer rings. In this work, θ_{max}, which is envisaged as a design input, is set to 0.7 rad so as to demonstrate the accuracy of the proposed device within the assumption of large deflections. However, by employing the same design framework, different θ_{max} values may be set as inputs to possibly synthesize zero torque CMs with an increased range of motion. Nonetheless, an extended motion range may be achieved only if larger stress, along with a lower accuracy of the reaction torques can be accepted. In addition, note that the design procedure reported in Sec. 2.3 has been hereafter employed to synthesize a proof-of-concept zero torque CM subjected to static loads only, hence neglecting possible fatigue issues.

3.1 Integrated Design Tool

To design the zero torque CM according to the models reported in Sec. 2, an integrated environment comprising Matlab and ANSYS APDL has been setup [35, 45]. The Matlab optimization toolbox is used to solve the analytical problem formulated in Sec. 2.3. Then, the obtained solution is verified via batch FEA analysis [49]. The general architecture of the proposed software framework, visible in Fig. 5, is organized in four main sections:

1. *Input Parameters*: in this section the user can specify all the input parameters (R_{in}, R_{ext}, E_{Sp}, E_N, n_N), the lower/upper bounds for the design variables (see Eq. 28), and the materials' elastic limit ($\sigma_{max,Sp}$, $\sigma_{max,N}$);
2. *Optimization*: in this section the optimization expressed by Eqs. 26-28 is solved by means of a gradient-based routine [50]. The behavioral model, characterized by the equations reported in Secs. 2.1-2.2, is stored in an exter-

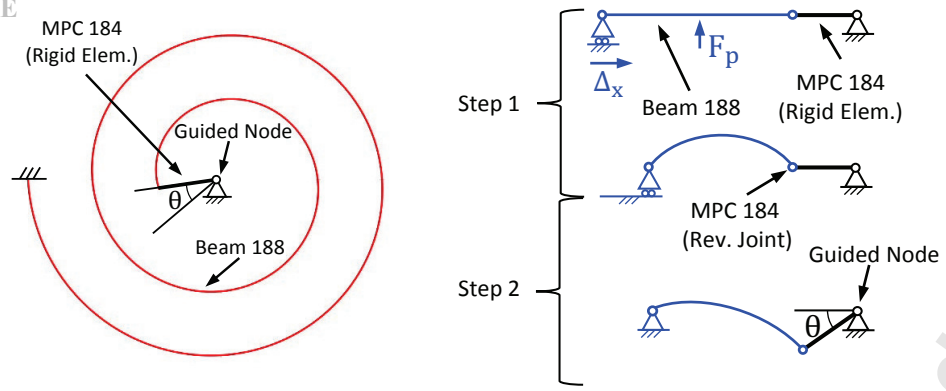

(a) Spiral 1D model - single step analysis.

(b) Negator 1D model - multi-step analysis.

Fig. 6: Representation of FE parametric models also depicting the element types.

nal function (OptFun.m), which provides the numerical value of M_{rms} for each of the candidates;

3. *FEA Batch Verification*: in this section the optimal configuration is tested via 1D batch FEA. Three separate APDL scripts are used to singularly investigate the behavior of the spiral, the negators and the overall zero torque mechanism. The optimal variables set, i.e. the one found in the previous section and composed of the entities visible in Eq. 28, is stored in an external file (FEA_Input.txt in Fig. 5) and then used to setup the FE models. All the scripts provide the automatic geometry generation, the meshing and the boundary conditions. The simulation outputs are saved by ANSYS in another external file (FEA_Output.txt in Fig. 5) and are then processed by Matlab;
4. *Results Comparison*: this section provides a list of the optimal variables set and a comparison between the outputs achieved with analytical and FEA models on the optimal configuration.

The FE models are shown in Fig. 6. All the beams are meshed with *Beam 188* elements (quadratic shape functions). *MPC 184* rigid elements are used both to model the rigid inner ring and, by setting *Keyopt(1)=6*, to create the revolute joint between the negator and the inner ring (see Fig. 6(b)). The spiral is analyzed in a single load-step by imposing a rotation θ to the central node and by fixing the other extremity, as in Fig. 6(a). The negator needs a multi-step approach: i) in the first load-step a displacement $\Delta_x = f$ and a perturbation force F_p are applied to the beam, as in Fig. 6(b), to obtain the pre-buckled state with a limited number of numerical iterations (substeps); ii) in the second load-step, F_p is removed and, as for the spiral model, the central node is guided in a rotation θ. As a direct output of the imposed rotation, the reaction torque and maximum Von Mises stress are evaluated and exported for both FE models.

3.2 Preliminary Study and Optimal Design

In the following, $R_{in} = 10$ mm and $R_{ext} = 50$ mm are considered. As for the materials, polypropylene and 1095 spring steel are adopted for the spiral and for the negators respectively. The Young's moduli are $E_{Sp} = 1450$ MPa and $E_N = 190000$ MPa, whereas the yield strengths are $\sigma_{Sp} = 50$ MPa and $\sigma_N = 950$ MPa.

Table 1: Analytical optimization results.

	Range	Opt. Value
b_{Sp}	$[1, 10]$ mm	6.33 mm
t_{Sp}	$[1, 10]$ mm	3.64 mm
b_N	$[1, 10]$ mm	2.12 mm
f	$[2.82, 10]$ mm	6.50 mm

Before considering the optimization process, a small parametric study has been conducted via the software framework in Fig. 5 on both the positive and the negative stiffness structures to validate the analytical formulations. By imposing $b_{Sp} = 10$ mm, $t_{Sp} = 3$ mm, $b_N = 10$ mm, $t_N = 1$ mm and by considering $E_{Sp} = E_N = 1450$ MPa, the effect of the spiral and of the single negator are analyzed via batch FEA for an imposed rotation $\theta = 0.7$ rad. The results are reported in Fig. 7. In particular, Fig. 7(a) reports the torque-deflection relationships achieved on the spiral for $1 \leq n_t \leq 10$, whereas Fig. 7(b) shows the single results of the negator with an imposed pre-buckling displacement $f = 6$ mm. The following considerations can be made:

- the analytical model captures the spiral's behavior accurately only for $n_t \geq 4$, as clearly shown in Figs. 7(a)-7(c)-7(d). The errors decrease as much as n_t increases;
- the analytical and FEA results match very well for the negator, as visible in Fig. 7(b). The torque-deflection relationship is affected by a rms error equal to 0.04 Nmm, and the maximum stresses differ of about 2.1%;
- the negator shows a remarkable loss in linearity for $\theta \geq 0.28$ rad.

On the basis of this discussion, $n_t = 4$ is considered to ensure accuracy in the analytical calculations and limit the spiral's

Journal of Mechanical Design. Received November 21, 2019;
Accepted manuscript posted March 14, 2020. doi:10.1115/1.4046810

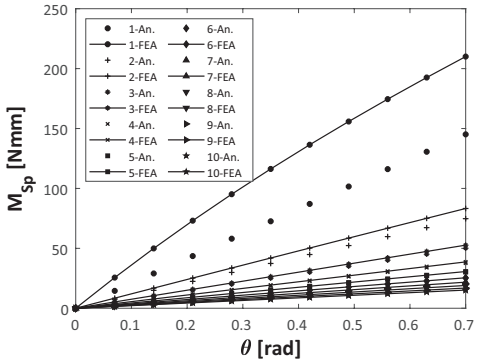

(a) Spiral: resulting M_{Sp} for different n_t.

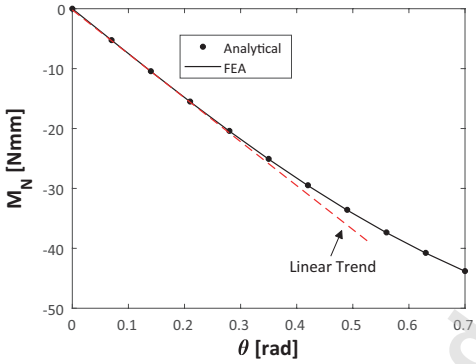

(b) Negator: resulting M_N.

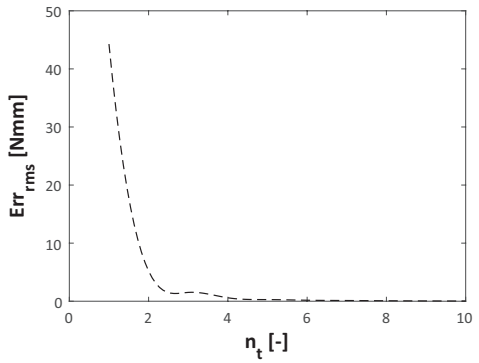

(c) Spiral: torque rms error for different n_t.

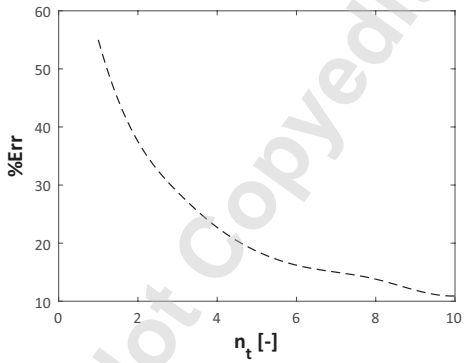

(d) Spiral: stress error (%) for different n_t.

Fig. 7: Comparison between analytical and FEA results for an imposed rotation $\theta = 0.7$ rad.

shape complexity within the radial range $[R_{in}, R_{ext}]$ in view of the manufacturing process. Moreover, since the negators are made of spring steel, it is convenient to cut a commercial sheet with a pre-defined size instead of trying to machine a precise thickness (i.e. the one obtained after the optimization). Consequently, by considering $t_N = 0.26$ mm, the design variables become b_{Sp}, t_{Sp}, b_N and f (see Eq. 28 without n_t and t_N). Imposed range of variation for each design variable and optimal values are summarized in Tab. 1. Wide ranges have been set for each design variable by considering the technological limits. Then, as specified in Sec. 2.3, Eq. 29 is used to define the lower bound for the variable f. A gradient-based interior-point algorithm (*fmincon*) has been set to solve the problem. Being the cost function non-convex in the design domain, in the attempt to avoid local minima, several starting points are considered in the optimization by adopting the *GlobalSearch* option within the *fmincon* routine. The simulations have been performed on a personal computer with an Intel(R) Core(TM) CPU @ 2.5 GHz and 16 GB RAM. The total elapsed time for the optimization study is 2.3 s. Then, each of the 1D batch FEA simulations in Fig. 5 took less than 15 s to be completed. Figure 8 reports the optimal configuration of the proposed CM. Overall, the results show good agreement. With reference to Fig. 8(c), both the analytical and FEA results are affected by an acceptable error with respect to the ideal zero torque characteristic, quantifiable as $M_{rms,An} = 1.33$ Nmm and $M_{rms,FEA} = 0.72$ Nmm. By comparing Fig. 8(a) and Fig. 8(b), these errors may be attributed to the difference between the spiral and negators characteristics. As highlighted in Fig. 7(b), the negators show an evident change in the trend for large deflections. On the contrary, the spiral behaves as a quasi-linear spring in the whole angular range. Therefore, a complete compensation cannot be achieved. The discrepancy between the analytical and the FEA data is mainly due to the slight differences between the behaviors shown in Fig. 8(a) (see also Fig. 7(c) with $n_t = 4$). Concerning the maximum stress, the spiral reached 3 MPa (3.94 MPa with FEA) at the maximum rotation $\theta = 0.7$ rad, and the negators reached 930 MPa (780 MPa with FEA) in the pre-loaded state. The CAD overview of the zero torque CM is shown in Fig. 8(d). A final FEA simulation has been performed to analyze the synthesized CM in the opposite direction, namely in the range $[-0.7, 0]$ rad, highlighting the following results:

- the Archimedean spiral (Fig. 2) provides a quasi-symmetric behavior when a rotation is enforced in either clockwise or anti-clockwise directions;
- the negator presents a symmetric behavior, as it may be expected by analyzing Eq. 17 and Fig. 4(c);
- the overall rms torque is equal to $M_{rms,FEA} = 0.73$ Nmm.

Therefore, the CM performance may be reasonably extended to the whole angular range, i.e. $[-0.7, 0.7]$ rad.

Journal of Mechanical Design. Received November 21, 2019;
Accepted manuscript posted March 14, 2020. doi:10.1115/1.4046810

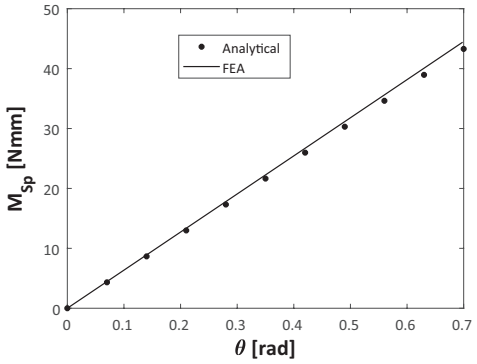

(a) Spiral Contribute.

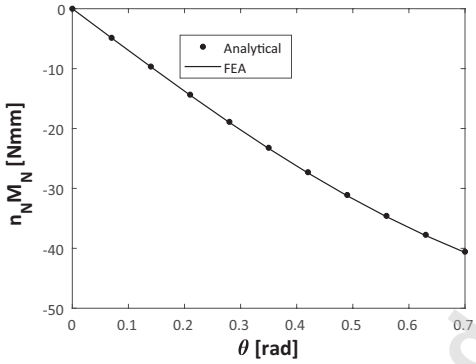

(b) Negators contribute ($n_N = 2$).

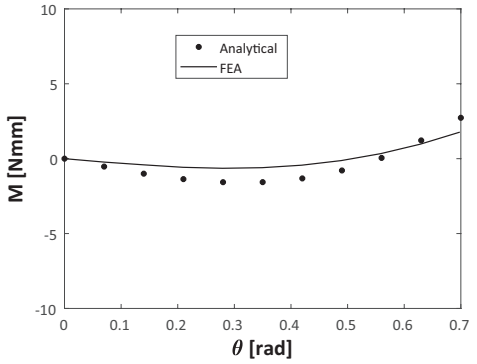

(c) Optimal torque-deflection relationship.

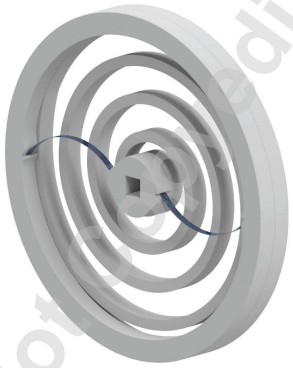

(d) Optimal design.

Fig. 8: Comparison between analytical and FEA results for an imposed rotation $\theta = 0.7$ rad.

4 FEA Shape Optimization

In the previous sections, a feasible design was presented. Simple analytical formulations can be used to synthesize a multi-material zero torque CM with a limited computational cost. However, as discussed in Sec. 3.2, a constant stiffness structure (as the one described by Eq. 10) cannot balance the negators for very large deflections. To overcome this issue, a second prototype is proposed where two spline beams are used in place of the spiral to balance the negators input. A more compact solution can be achieved with all the elements in a single annular frame ($R_{in} = 10$ mm, $R_{ext} = 50$ mm), as shown in Fig. 1(a). The aim is to reduce the rms torque (i.e. M_{rms}) in the operative range $[0, 0.7]$ rad. By adopting the previous optimal negators, whose dimensions are reported in Sec. 3.2, two identical spline beams that provide a response symmetric to the one reported in Fig. 8(b) have been synthesized. The behavior of spline beams undergoing large deflections cannot be easily modeled via theoretical approaches. Hence, a FEA optimization is carried out to generate spline beams that match a prescribed torque-deflection characteristic [4, 44, 51, 52]. The study is performed using the framework visible in Fig. 9, namely a simplified version of the one shown in Fig. 5. A Matlab script manages the optimization (pre/post-processing and ANSYS batch execution), whereas ANSYS APDL is used to provide the torque-deflection relationship of each candidate and the maximum Von Mises stress. The objective function is calculated in Matlab as follows:

$$e_{rms} = \sqrt{\frac{1}{r}\sum_{i=1}^{r}\left[|M_{N_i}| - M_i\right]^2} \tag{30}$$

where e_{rms} is the rms value of the error between the reference behavior, namely the one in Fig. 8(b) reversed in the positive plane, and the i-th FEA response (i.e. M_i). The number of substeps, r, is set equal to 10. The FE parametric model is shown in Fig. 10: the beam axis is defined by a cubic spline [4] that is forced to pass through a set of six interpolation points (p_{in}, p_1, p_2, p_3, p_4, p_{ext}). Note that p_{in} and p_{ext} are placed to the inner and outer ring respectively, thus only their characteristic angle must be considered in the optimization. As compared to straight segments, the use of spline functions ensure lower stress concentrations where the structure undergoes changes in the curvature [4, 44]. The spline beam is made with polypropylene and is characterized by a constant cross section, defined by width b_b and thickness t_b. The new design variables are:

- b_b and t_b $\rightarrow$ cross sections' dimensions;
- r_{p_i}, $i = 1, .., 4$ $\rightarrow$ radius of each interpolation point;
- φ_{p_i}, $i = 1, .., 4$, $\varphi_{p_{in}}$, $\varphi_{p_{ext}}$ $\rightarrow$ angle of each interpolation point.

Journal of Mechanical Design. Received November 21, 2019;
Accepted manuscript posted March 14, 2020. doi:10.1115/1.4046810

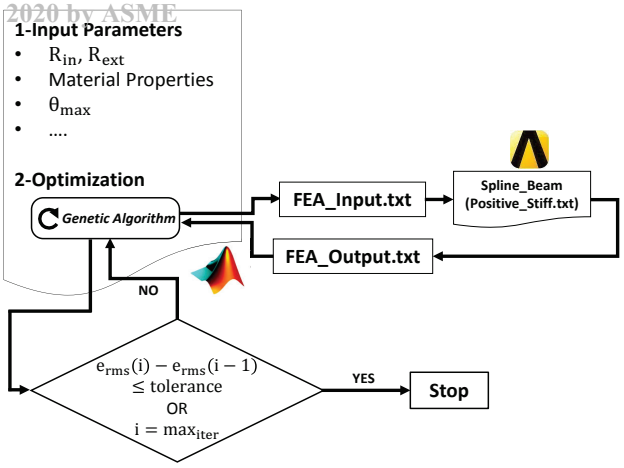

Fig. 9: Shape optimization framework.

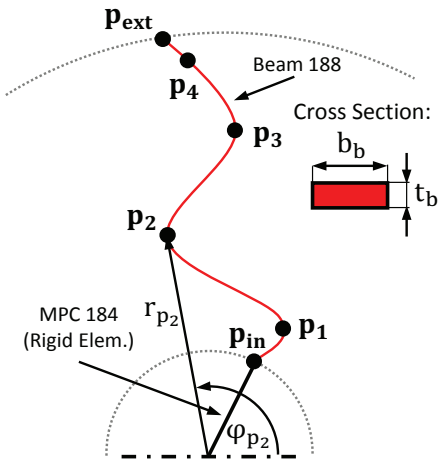

Fig. 10: Representation of the FE parametric model (with element type) for the shape optimization process.

In line with the previous optimization study (see Eqs. 26-28), a constraint on the maximum stress is added to the algorithm to exclude all the candidates that exceed the yield strength (55 MPa) during the simulation. To increase the computational efficiency, a single spline beam is parametrized and then tested with FEA. Differently from the optimization problem reported in Sec. 2.3, which leverages analytical models, in the current procedure an explicit correlation between the design variables and the cost function is not available. An approximate correlation, namely a surrogate model, may be retrieved by means of the design of experiments and the response surface modeling techniques [50]. However, the large number of design variables would considerably increase the total number of FEA simulations to be performed, especially if the full-factorial discretization is adopted. On the contrary, genetic algorithms do not provide as an output the aforementioned correlation but they can manage a very large number of design variables and they converge after a relatively limited number of iterations. Therefore, on the basis of the results presented in [4, 44, 52] for similar devices, in this work, a genetic algorithm has been used to optimize

Table 2: Shape optimization results.

	Range	Opt. Value
b_b	$[1,10]$ mm	3.81 mm
t_b	$[0.5,5]$ mm	0.80 mm
r_{p_1}	$[11,21]$ mm	13.29 mm
r_{p_2}	$[22,26]$ mm	25.00 mm
r_{p_3}	$[27,32]$ mm	28.21 mm
r_{p_4}	$[33,49]$ mm	35.00 mm
φ_{p_1}	$[1,2.5]$ rad	1.61 rad
φ_{p_2}	$[1,2.5]$ rad	1.56 rad
φ_{p_3}	$[1,2.5]$ rad	1.40 rad
φ_{p_4}	$[1,2.5]$ rad	1.13 rad
$\varphi_{p_{in}}$	$[1,2.5]$ rad	1.77 rad
$\varphi_{p_{ext}}$	$[1,2.5]$ rad	1.75 rad

the shape of the spline beams.

The optimization has been run with 100 generations and 30 candidates for each generation. Each batch FEA takes $3-5$ s to be completed in ANSYS. By adopting a function tolerance equal to 10^{-4}, the convergence has been reached after 90 generations and total time equal to 180 min. The optimal variables set, reported in Tab. 2, allows to match the negator trend with good accuracy, as visible in Fig. 11(a), which shows the contributions of both the spline beams in parallel spring configuration. The final torque-deflection relationship, resulting from the new stiffness compensation, is reported in Fig. 11(b). The overall rms torque has been significantly reduced with respect to the prototype in Fig. 8(d), i.e. from $M_{rms,FEA} = 0.72$ Nmm to $M_{rms,FEA} = 0.30$ Nmm. As a drawback, the asymmetric behavior of the spline beams limits the use of the second prototype in the range $[0, 0.7]$ rad. However, by setting any intermediate positions as reference position, the CM can be utilized in both directions. The new mechanism is shown in Fig. 11(c). The maximum stress acting on the spline beams is equal to 39 MPa for a deflection of $\theta = 0.7$ rad.

5 Experimental validation

Physical prototypes have been fabricated and tested to validate the predicted torque-deflection behaviors. By nature, CMs can be difficult to produce using both additive and subtraction manufacturing methods. Conventional and climb milling, as well as 3D printing (fused deposition modeling) often result in unacceptable variation when creating thin members. Therefore, the annular frames, the spiral and the spline beams have been manufactured by means of a 3-axis Haas DM1 CNC machine. In line with the calculation, the specimens are made of polypropylene whereas the nega-

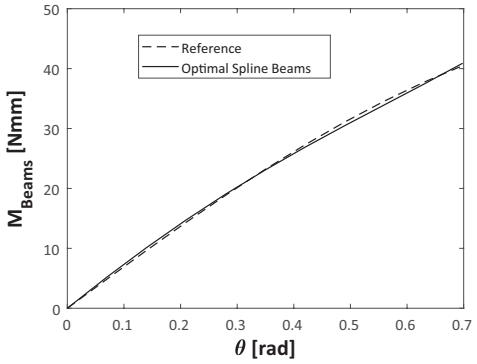

(a) Comparison between optimal spline contribute and reference behavior (absolute value of the negators contribute).

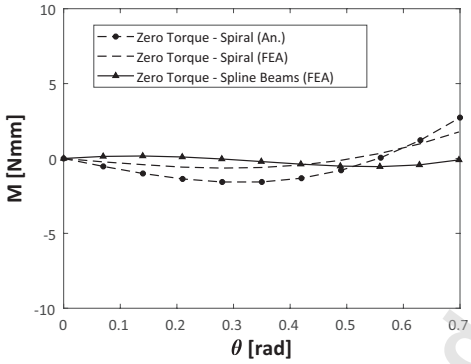

(b) Zero torque CM - comparison between prototypes.

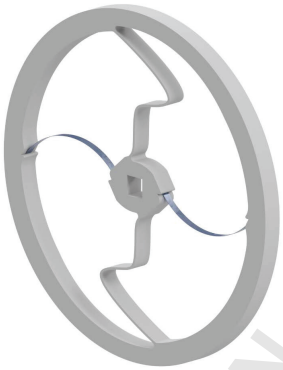

(c) Optimal design.

Fig. 11: Shape optimization results for an imposed rotation $\theta = 0.7$ rad.

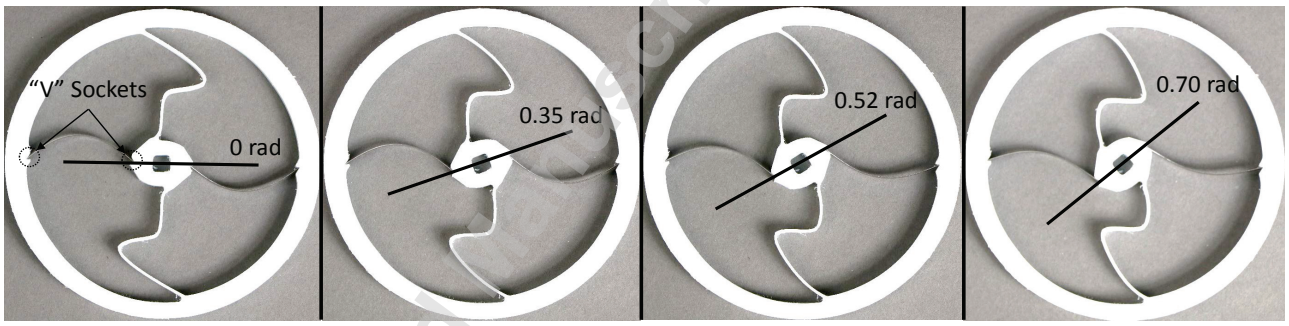

Fig. 12: Second prototype - static balancing in different angular positions.

tors are cut from a commercial spring steel sheet (0.26 mm thick). The negator pins are realized by direct contact of the thin beam against "V" sockets cut into the inner and outer rings. The pre-loaded condition, shown in Fig. 4(b), is realized by fixing both rings to the ground and by imposing the axial displacement, f, to the beams.

The high accuracy of the machined parts can be seen in Fig. 12, which shows a complete balancing of the second prototype for different angular positions in the range $[0, 0.7]$ rad. It should be noted that the spline beams ensure the vertical stability in the undeflected configuration with $n_N = 2$, limiting the need of a central pin to the first prototype only.

Both the specimens have been tested with the experimental setup shown in Fig. 13. The system is composed of a worm-wheel gearset that acts on a shaft, an Omega TQ103 socket torque gauge and a US Digital optical encoder. A shape coupling is used to connect the shaft extremity with the inner ring. The outer ring is then fixed to the ground through a connection member (shown in Fig. 13). The shaft is manually actuated and both angular position and reaction torque are acquired using a Labview interface. The results of the test are plotted in Fig. 14. FEA and the experimental data show good agreement for both prototypes, confirming the accuracy of the proposed modeling approach. The discrepancy

Journal of Mechanical Design. Received November 21, 2019;
Accepted manuscript posted March 14, 2020. doi:10.1115/1.4046810

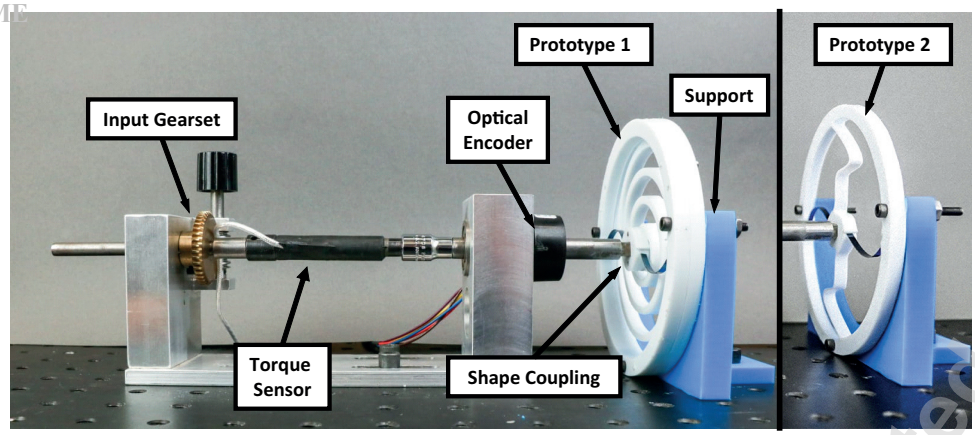

Fig. 13: Experimental setup. The two images show the rotational test on both the prototypes.

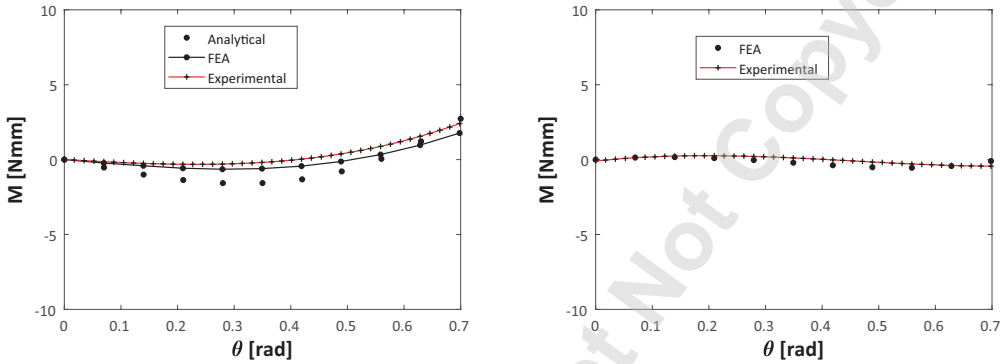

(a) First Prototype.

(b) Second Prototype.

Fig. 14: Comparison between predicted and measured behaviors.

between the data may be mainly due to:

- small defects in the machined parts;
- uncertainties in the material properties;
- the FE model (mesh quality and settings);
- the non-ideal pins (contact between the negators and the "V" sockets);
- the user's irregular action during the manual deflection of the specimens.

6 Conclusions

This paper presents innovative concepts for a compact zero torque CM and illustrates their design. Statically balanced CMs have been presented in literature, although their size and shape do not allow for easy or practical implementation. The proposed device consists of a simple annular frame to maximize its applicability and scalability. The system is synthesized by exploiting the stiffness compensation method, i.e. by adopting elastic elements that provide opposite responses in terms of reaction torque for an imposed rotation. Pinned-pinned pre-buckled beams between the inner and the outer rings of the frame are used as negators. Two prototypes are presented, modeled and optimized to obtain the zero output between $\theta = 0$ rad and $\theta = 0.7$ rad. The first prototype combines the effects of an Archimedean spiral and of a set of two pre-buckled beams. Analytical models for both the spiral and the negators are provided. An integrated tool comprising Matlab and ANSYS is developed to design the mechanism.

The analytical and FEA data are consistent and the overall behavior is quasi-symmetric for positive and negative rotations of the inner ring. However, the negators show a remarkable nonlinear trend for large deflections (an evident loss in linearity after $\theta \geq 0.28$ rad), limiting the accuracy of overall mechanism output.

As an attempt to reduce the compensation error and to further increase the mechanism compactness, a second prototype has been proposed. In particular, a set of two spline beams are employed in place of the spiral to obtain a nonlinear positive spring capable of counteracting the negators. The shape and size of the spline beams have been optimized via a genetic algorithm and batch FEA simulations. As a result of the numerical optimization, the accuracy of the zero torque mechanism significantly increased. However, the asymmetric behavior of the spline beams limits the use of the second prototype in the pre-defined interval.

Lastly, physical prototypes have been produced with a 3-axis CNC machine and tested with a rotational setup. The ac-

quired torque-deflection relationships matched with the predicted behaviors and confirmed the validity of the proposed design approach.

7 Funding Sources

The research has received funding from University of Genova grant - COSMET, COmpliant Shell-based mechanisms for MEdical Technologies.

References

[1] Howell, L. L., 2001. *Compliant mechanisms*. John Wiley & Sons.

[2] Hou, C.-W., and Lan, C.-C., 2013. "Functional joint mechanisms with constant-torque outputs". *Mechanism and Machine Theory,* **62**, pp. 166–181.

[3] Lan, C.-C., and Wang, J.-Y., 2011. "Design of adjustable constant-force forceps for robot-assisted surgical manipulation". *IEEE International Conference on Robotics and Automation (ICRA)*, pp. 386–391.

[4] Prakashah, H. N., and Zhou, H., 2016. "Synthesis of constant torque compliant mechanisms". *Journal of Mechanisms and Robotics,* **8**(6), p. 064503.

[5] Reddy, B. P., and Zhou, H., 2017. "Synthesizing bidirectional constant torque compliant mechanisms". *ASME International Mechanical Engineering Congress and Exposition (IMECE)*, pp. V04AT05A006–V04AT05A006.

[6] Gandhi, I., and Zhou, H., 2019. "Synthesizing constant torque compliant mechanisms using precompressed beams". *Journal of Mechanical Design,* **141**(1), p. 014501.

[7] Wang, P., Yang, S., and Xu, Q., 2018. "Design and optimization of a new compliant rotary positioning stage with constant output torque". *International Journal of Precision Engineering and Manufacturing,* **19**(12), pp. 1843–1850.

[8] Brown, A., 1981. *Engineering Design Guides (Mechanical Springs) 42*. Oxford University Press.

[9] Xu, Q., 2017. "Design of a large-stroke bistable mechanism for the application in constant-force micropositioning stage". *Journal of Mechanisms and Robotics,* **9**(1), p. 011006.

[10] Wang, P., and Xu, Q., 2017. "Design and testing of a flexure-based constant-force stage for biological cell micromanipulation". *Transactions on Automation Science and Engineering,* **15**(3), pp. 1114–1126.

[11] Wang, J.-Y., and Lan, C.-C., 2014. "A constant-force compliant gripper for handling objects of various sizes". *Journal of Mechanical Design,* **136**(7), p. 071008.

[12] Tolman, K. A., Merriam, E. G., and Howell, L. L., 2016. "Compliant constant-force linear-motion mechanism". *Mechanism and Machine Theory,* **106**, pp. 68–79.

[13] Chen, Y.-H., and Lan, C.-C., 2012. "An adjustable constant-force mechanism for adaptive end-effector operations". *Journal of Mechanical Design,* **134**(3), p. 031005.

[14] López-Martínez, J., García-Vallejo, D., Arrabal-Campos, F. M., and Garcia-Manrique, J. M., 2018. "Design of three new cam-based constant-force mechanisms". *Journal of Mechanical Design,* **140**(8), p. 082302.

[15] Berselli, G., Mammano, G. S., and Dragoni, E., 2014. "Design of a dielectric elastomer cylindrical actuator with quasi-constant available thrust: modeling procedure and experimental validation". *Journal of Mechanical Design,* **136**(12), p. 125001.

[16] Pedersen, C., Fleck, N., and Ananthasuresh, G., 2006. "Design of a compliant mechanism to modify an actuator characteristic to deliver a constant output force". *Journal of Mechanical Design,* **128**(5), pp. 1101–1112.

[17] Wang, P., and Xu, Q., 2018. "Design and modeling of constant-force mechanisms: A survey". *Mechanism and Machine Theory,* **119**, pp. 1–21.

[18] McGuire, J. R., 1996. "Analysis and design of constant-torque springs used in aerospace applications.". *PhD Dissertation, The University of Texas at Austin*.

[19] Arakelian, V., and Ghazaryan, S., 2008. "Improvement of balancing accuracy of robotic systems: application to leg orthosis for rehabilitation devices". *Mechanism and Machine Theory,* **43**(5), pp. 565–575.

[20] Chew, D. X., Wood, K. L., and Tan, U.-X., 2019. "Design of a passive self-regulating gravity compensator for variable payloads". *Journal of Mechanical Design,* **141**(10), p. 102302.

[21] Wu, Y.-S., and Lan, C.-C., 2014. "Linear variable-stiffness mechanisms based on preloaded curved beams". *Journal of Mechanical Design,* **136**(12), p. 122302.

[22] Scirè Mammano, G., and Dragoni, E., 2014. "Elastic compensation of linear shape memory alloy actuators using compliant mechanisms". *Journal of Intelligent Material Systems and Structures,* **25**(9), pp. 1124–1138.

[23] Ma, F., and Chen, G., 2017. "Bi-BCM: A closed-form solution for fixed-guided beams in compliant mechanisms". *Journal of Mechanisms and Robotics,* **9**(1), p. 014501.

[24] Hao, G., and Mullins, J., 2016. "On the comprehensive static characteristic analysis of a translational bistable mechanism". *Proceedings of the Institution of Mechanical Engineers, Part C: Journal of Mechanical Engineering Science,* **230**(20), pp. 3803–3817.

[25] Morsch, F. M., and Herder, J. L., 2010. "Design of a generic zero stiffness compliant joint". *ASME International Design Engineering Technical Conferences and Computers and Information in Engineering Conference (IDETC/CIE)*, pp. 427–435.

[26] Herder, J. L., 2001. *Energy-free Systems. Theory, conception and design of statically*, Vol. 2.

[27] Sangamesh, D., 2012. "Static balancing of rigid-body linkages and compliant mechanisms". *Indian Institute of Science Bangalore*.

[28] Merriam, E. G., and Howell, L. L., 2015. "Non-dimensional approach for static balancing of rotational

flexures". *Mechanism and Machine Theory,* **84**, pp. 90–98.

[29] Radaelli, G., Gallego, J. A., and Herder, J. L., 2011. "An energy approach to static balancing of systems with torsion stiffness". *Journal of Mechanical Design,* **133**(9), p. 091006.

[30] Stapel, A., and Herder, J. L., 2004. "Feasibility study of a fully compliant statically balanced laparoscopic grasper". *ASME International Design Engineering Technical Conferences and Computers and Information in Engineering Conference (IDETC/CIE)*, pp. 635–643.

[31] Merriam, E. G., Tolman, K. A., and Howell, L. L., 2016. "Integration of advanced stiffness-reduction techniques demonstrated in a 3D-printable joint". *Mechanism and Machine Theory,* **105**, pp. 260–271.

[32] Zhao, H., Zhao, C., Ren, S., and Bi, S., 2019. "Analysis and evaluation of a near-zero stiffness rotational flexural pivot". *Mechanism and Machine Theory,* **135**, pp. 115–129.

[33] Berselli, G., Guerra, A., Vassura, G., and Andrisano, A. O., 2014. "An engineering method for comparing selectively compliant joints in robotic structures". *Transactions on Mechatronics,* **19**(6), pp. 1882–1895.

[34] Hongzhe, Z., and Shusheng, B., 2010. "Accuracy characteristics of the generalized cross-spring pivot". *Mechanism and Machine Theory,* **45**(10), pp. 1434–1448.

[35] Bilancia, P., Berselli, G., Magleby, S., and Howell, L., 2020. "On the modeling of a contact-aided cross-axis flexural pivot". *Mechanism and Machine Theory,* **143**, p. 103618.

[36] C-Flex Bearing Co., Inc. https://c-flex.com/. Accessed: 2020-01-05.

[37] Howell, L. L., Magleby, S. P., Olsen, B. M., and Wiley, J., 2013. *Handbook of compliant mechanisms*. Wiley Online Library.

[38] Rubbert, L., Caro, S., Gangloff, J., and Renaud, P., 2014. "Using singularities of parallel manipulators to enhance the rigid-body replacement design method of compliant mechanisms". *Journal of Mechanical Design,* **136**(5), p. 051010.

[39] Melchiorri, C., Palli, G., Berselli, G., and Vassura, G., 2013. "Development of the ub hand iv: Overview of design solutions and enabling technologies". *Robotics & Automation Magazine,* **20**(3), pp. 72–81.

[40] Herder, J. L., 1998. "Design of spring force compensation systems". *Mechanism and Machine Theory,* **33**(1-2), pp. 151–161.

[41] Tolou, N., Smit, G., Nikooyan, A. A., Plettenburg, D. H., and Herder, J. L., 2012. "Stiffness compensation mechanism for body powered hand prostheses with cosmetic covering". *Journal of Medical Devices,* **6**(1), p. 011004.

[42] Knox, B. T., and Schmiedeler, J. P., 2009. "A unidirectional series-elastic actuator design using a spiral torsion spring". *Journal of Mechanical Design,* **131**(12), p. 125001.

[43] Scarcia, U., Berselli, G., Melchiorri, C., Ghinelli, M., and Palli, G., 2016. "Optimal design of 3D printed spiral torsion springs". *ASME Conference on Smart Materials, Adaptive Structures and Intelligent Systems (SMASIS)*, pp. V002T03A020–V002T03A020.

[44] Jutte, C. V., and Kota, S., 2008. "Design of nonlinear springs for prescribed load-displacement functions". *Journal of Mechanical Design,* **130**(8), p. 081403.

[45] Bilancia, P., Berselli, G., Bruzzone, L., and Fanghella, P., 2019. "A CAD/CAE integration framework for analyzing and designing spatial compliant mechanisms via pseudo-rigid-body methods". *Robotics and Computer-Integrated Manufacturing,* **56**, pp. 287–302.

[46] Muñoz-Guijosa, J. M., Caballero, D. F., de la Cruz, V. R., Sanz, J. L. M., and Echávarri, J., 2012. "Generalized spiral torsion spring model". *Mechanism and Machine Theory,* **51**, pp. 110–130.

[47] Furnémont, R., Mathijssen, G., Van Der Hoeven, T., Brackx, B., Lefeber, D., and Vanderborght, B., 2015. "Torsion MACCEPA: A novel compact compliant actuator designed around the drive axis". *IEEE International Conference on Robotics and Automation (ICRA)*, pp. 232–237.

[48] Timoshenko, S. P., and Gere, J. M., 2009. *Theory of elastic stability*. Courier Corporation.

[49] ANSYS, 2016. *ANSYS Mechanical User's Guide*. ANSYS, Inc, Canonsburg, Pennsylvania.

[50] Cavazzuti, M., 2012. *Optimization methods: from theory to design scientific and technological aspects in mechanics*. Springer Science & Business Media.

[51] Bilancia, P., Berselli, G., Scarcia, U., and Palli, G., 2018. "Design of a beam-based variable stiffness actuator via shape optimization in a CAD/CAE environment". *ASME Conference on Smart Materials, Adaptive Structures and Intelligent Systems (SMASIS)*.

[52] Cheng, Z., Foong, S., Sun, D., and Tan, U.-X., 2014. "Algorithm for design of compliant mechanisms for torsional applications". *IEEE International Conference on Advanced Intelligent Mechatronics (AIM)*, pp. 628–633.